

SECOND SEASON QUIET OBSERVATIONS: MEASUREMENTS OF THE CMB POLARIZATION POWER SPECTRUM AT 95 GHz

QUIET COLLABORATION — D. ARAUJO¹, C. BISCHOFF^{2,3}, A. BRIZIUS^{2,4}, I. BUDER^{2,3}, Y. CHINONE^{5,6}, K. CLEARY⁷,
 R. N. DUMOULIN¹, A. KUSAKA^{2,8}, R. MONSALVE⁹, S. K. NÆSS¹⁰, L. B. NEWBURGH^{1,8}, R. REEVES⁷, I. K. WEHUS^{11,12},
 J. T. L. ZWART^{1,13}, L. BRONFMAN¹⁴, R. BUSTOS^{9,14,15}, S. E. CHURCH¹⁶, C. DICKINSON¹⁷, H. K. ERIKSEN^{10,18}, T. GAIER¹⁹,
 J. O. GUNDERSEN⁹, M. HASEGAWA⁵, M. HAZUMI⁵, K. M. HUFFENBERGER⁹, K. ISHIDOSHIO⁵, M. E. JONES¹¹,
 P. KANGASLAHTI¹⁹, D. J. KAPNER^{2,20}, D. KUBIK²¹, C. R. LAWRENCE¹⁹, M. LIMON¹, J. J. MCMAHON²², A. D. MILLER¹,
 M. NAGAI⁵, H. NGUYEN²¹, G. NIXON^{8,23}, T. J. PEARSON⁷, L. PICCIRILLO¹⁷, S. J. E. RADFORD⁷, A. C. S. READHEAD⁷,
 J. L. RICHARDS⁷, D. SAMTLEBEN^{4,24}, M. SEIFFERT¹⁹, M. C. SHEPHERD⁷, K. M. SMITH^{2,8}, S. T. STAGGS⁸, O. TAJIMA^{2,5},
 K. L. THOMPSON¹⁶, K. VANDERLINDE^{2,25}, R. WILLIAMSON^{1,2}

Submitted to ApJ—This paper should be cited as “QUIET Collaboration (2012)”

ABSTRACT

The Q/U Imaging Experiment (QUIET) has observed the cosmic microwave background (CMB) at 43 and 95 GHz. The 43-GHz results have been published in QUIET Collaboration et al. (2011), and here we report the measurement of CMB polarization power spectra using the 95-GHz data. This data set comprises 5337 hours of observations recorded by an array of 84 polarized coherent receivers with a total array sensitivity of $87 \mu\text{K}\sqrt{\text{s}}$. Four low-foreground fields were observed, covering a total of ~ 1000 square degrees with an effective angular resolution of $12'8$, allowing for constraints on primordial gravitational waves and high-signal-to-noise measurements of the E -modes across three acoustic peaks. The data reduction was performed using two independent analysis pipelines, one based on a pseudo- C_ℓ (PCL) cross-correlation approach, and the other on a maximum-likelihood (ML) approach. All data selection criteria and filters were modified until a predefined set of null tests had been satisfied before inspecting any non-null power spectrum. The results derived by the two pipelines are in good agreement. We characterize the EE , EB and BB power spectra between $\ell = 25$ and 975 and find that the EE spectrum is consistent with ΛCDM , while the BB power spectrum is consistent with zero. Based on these measurements, we constrain the tensor-to-scalar ratio to $r = 1.1^{+0.9}_{-0.8}$ ($r < 2.8$ at 95% C.L.) as derived by the ML pipeline, and $r = 1.2^{+0.9}_{-0.8}$ ($r < 2.7$ at 95% C.L.) as derived by the PCL pipeline. In one of the fields, we find a correlation with the dust component of the Planck Sky Model, though the corresponding excess power is small compared to statistical errors. Finally, we derive limits on all known systematic errors, and demonstrate that these correspond to a tensor-to-scalar ratio smaller than $r = 0.01$, the lowest level yet reported in the literature.

Subject headings: cosmic background radiation—Cosmology: observations—Gravitational waves—
 inflation—Polarization

¹ Department of Physics and Columbia Astrophysics Laboratory, Columbia University, New York, NY 10027, USA

² Kavli Institute for Cosmological Physics, Department of Physics, Enrico Fermi Institute, The University of Chicago, Chicago, IL 60637, USA; send correspondence to I. Buder, ibuder@uchicago.edu

³ Harvard-Smithsonian Center for Astrophysics, 60 Garden Street MS 43, Cambridge, MA 02138, USA

⁴ Max-Planck-Institut für Radioastronomie, Auf dem Hügel 69, 53121 Bonn, Germany

⁵ High Energy Accelerator Research Organization (KEK), 1-1 Oho, Tsukuba, Ibaraki 305-0801, Japan

⁶ Astronomical Institute, Graduate School of Science, Tohoku University, Aramaki, Aoba, Sendai 980-8578, Japan

⁷ Cahill Center for Astronomy and Astrophysics, California Institute of Technology, 1200 E. California Blvd M/C 249-17, Pasadena, CA 91125, USA

⁸ Joseph Henry Laboratories of Physics, Jadwin Hall, Princeton University, Princeton, NJ 08544, USA

⁹ Department of Physics, University of Miami, 1320 Campo Sano Drive, Coral Gables, FL 33146, USA

¹⁰ Institute of Theoretical Astrophysics, University of Oslo, P.O. Box 1029 Blindern, N-0315 Oslo, Norway

¹¹ Department of Astrophysics, University of Oxford, Keble Road, Oxford OX1 3RH, UK

¹² Department of Physics, University of Oslo, P.O. Box 1048 Blindern, N-0316 Oslo, Norway

¹³ Physics Department, University of the Western Cape, Pri-

vate Bag X17, Bellville 7535, South Africa

¹⁴ Departamento de Astronomía, Universidad de Chile, Casilla 36-D, Santiago, Chile

¹⁵ Departamento de Astronomía, Universidad de Concepción, Casilla 160-C, Concepción, Chile

¹⁶ Kavli Institute for Particle Astrophysics and Cosmology and Department of Physics, Stanford University, Varian Physics Building, 382 Via Pueblo Mall, Stanford, CA 94305, USA

¹⁷ Jodrell Bank Centre for Astrophysics, Alan Turing Building, School of Physics and Astronomy, The University of Manchester, Oxford Road, Manchester M13 9PL, UK

¹⁸ Centre of Mathematics for Applications, University of Oslo, P.O. Box 1053 Blindern, N-0316 Oslo, Norway

¹⁹ Jet Propulsion Laboratory, California Institute of Technology, 4800 Oak Grove Drive, Pasadena, CA, USA 91109

²⁰ Micro Encoder Inc., Kirkland, WA 98034, USA

²¹ Fermi National Accelerator Laboratory, Batavia, IL 60510, USA

²² Department of Physics, University of Michigan, 450 Church Street, Ann Arbor, MI 48109, USA

²³ Tradeworx, Inc., 10 Broad Street, Third Floor, Red Bank, NJ 07701, USA

²⁴ Nikhef, Science Park, Amsterdam, The Netherlands

²⁵ Department of Physics, McGill University, 3600 Rue University, Montreal, Quebec H3A 2T8, Canada

1. INTRODUCTION

The theory of inflation explains several well-observed properties of the Universe (e.g. Liddle & Lyth 2000, and references therein): the lack of spatial curvature, the absence of relic monopoles from a grand unified theory’s broken symmetry, the large-scale correlations that imply a much larger particle horizon than the Big Bang scenario provides without inflation, and the nearly-scale-invariant Gaussian fluctuations. Although inflation was developed to explain these known properties of the Universe, which are now probed with high precision by recent cosmological observations (Komatsu et al. 2011; Dunkley et al. 2011; Keisler et al. 2011; Anderson et al. 2012; Hicken et al. 2009; Kessler et al. 2009; Roza et al. 2010), the model also has a new feature: the early, exponential expansion of space generates a stochastic background of gravitational waves. In the near term, polarization measurements of the cosmic microwave background (CMB) present the most promising approach to detect these gravitational waves, which cause an odd-parity (B -mode) polarization pattern on angular scales larger than a degree (Seljak & Zaldarriaga 1997; Kamionkowski et al. 1997). Detection (or non-detection) of these patterns will place strong constraints on the inflation paradigm.

In the slow-roll approximation (for a review see Liddle & Lyth 2000), the B -mode intensity is parametrized by the tensor-to-scalar ratio r , which is related to the energy scale V of inflation by $V \sim (r/0.01)^{1/4} \times 10^{16}$ GeV. For many classes of inflationary models, r can be as large as $0.01 \lesssim r \lesssim 0.1$ (Boyle et al. 2006).

A combination of CMB-temperature-anisotropy measurements, baryon-acoustic-oscillation data, and supernova observations has given the most stringent limit to date, $r \lesssim 0.2$ at 95% confidence level (C.L.), nearly limited by cosmic variance (Komatsu et al. 2011; Keisler et al. 2011; Dunkley et al. 2011). In order to improve on these constraints significantly, direct observations of CMB polarization are required. Thus far the best limit from CMB polarization alone is $r < 0.72$ at 95% C.L. (Chiang et al. 2010), while many experiments have observed even-parity patterns (E -modes) (Leitch et al. 2005; Montroy et al. 2006; Sievers et al. 2007; Wu et al. 2007; Bischoff et al. 2008; Brown et al. 2009; Larson et al. 2011; QUIET Collaboration et al. 2011).

The Q/U Imaging Experiment (QUIET) observed the CMB from the ground between 2008 October and 2010 December. The observation site was the Chajnantor plateau at an altitude of 5080m in the Atacama Desert in Chile. Two different receivers were employed, corresponding to center frequencies of 43 (Q-band) and 95 GHz (W-band). The results of the 43-GHz measurements have been published in QUIET Collaboration et al. (2011) and included a measurement of the E -mode power spectrum between $\ell = 25$ and 475 and an upper limit on the tensor-to-scalar ratio of $r < 2.1$ at 95% C.L. In this paper, we report measurements of the CMB polarization power spectra for the 95-GHz data. We note that this experiment played the role of a pathfinder, demonstrating that monolithic-microwave-integrated-circuit (MMIC) arrays are capable

of controlling systematic errors and achieving the sensitivity required to reach $r \lesssim 0.01$.

QUIET was led by Bruce Winstein, who died in 2011 February soon after observations were completed. His intellectual and scientific guidance was crucial to the experiment’s success.

2. INSTRUMENT

In this section, we summarize the salient features of the 95-GHz instrument. For further details, we refer to separate papers (QUIET Collaboration et al. 2011; QUIET Collaboration 2012), hereafter referred to as QUIET 2011 and QUIET 2012, respectively. Additional information on the QUIET instrument is provided in Bischoff (2010); Brizius (2011); Cleary (2010); Kusaka (2010); Monsalve (2010); Newburgh (2010, 2012); and Reeves (2012).

The QUIET telescope consists of a 1.4-m side-fed classical Dragonian antenna that satisfies the Mizuguchi condition (QUIET 2012). The Cosmic Background Imager (CBI) telescope mount was reused for the QUIET project. It provides three-axis motion: azimuth, elevation, and rotation about the optical axis, called “deck” rotation (Padin et al. 2002). The 95-GHz receiver comprises 84 polarization-sensitive radiometers and six radiometers with differential-temperature sensitivity. The array sensitivity is $87 \mu\text{K}\sqrt{\text{s}}$ to the CMB polarization. The instantaneous angular resolution is $11.7'$ in full width at half maximum (FWHM). The telescope field of view is roughly circular with a diameter of $\sim 8^\circ$.

The coherent QUIET radiometers directly measure the Stokes Q and U parameters (QUIET 2011; QUIET 2012). The intensity, I , is also recorded by the same radiometers, but with significantly higher noise. One of the strengths of the QUIET design is excellent immunity to both $1/f$ noise from gain fluctuations and instrumental spurious polarization (hereafter I -to- Q/U leakage). The median $1/f$ knee frequency of the radiometers is 10 mHz, significantly below the typical scan frequency of 45–100 mHz, resulting in a negligible $1/f$ noise contribution. The fractional I -to- Q/U leakages are 0.2% for the monopole component, 0.4% for the dipole component, and 0.2% for the quadrupole component (QUIET 2012).

The receiver and telescope mirrors are surrounded by an absorptive ground screen, eliminating major contributions from the 300-K ground emission. The upper component of the ground screen was installed in 2010 January and eliminated two localized far sidelobes with intensities ~ -60 dB (QUIET 2012), which existed during the first few months of operation (from 2009 August through 2010 January). For the data from the early part of the season, we reject the part where the Sun entered either of these sidelobes. Scan-synchronous signal due to ground emission is projected out of the maps in the analysis (QUIET 2011). Possible remaining effects are estimated as a systematic error (Section 5.3).

3. OBSERVATIONS

With the 95-GHz receiver, we observed from 2009 August 12 until 2010 December 22 and accumulated 7426 hours of data²⁶. Of these data, 72% were spent

²⁶ The instrument was in the nominal CMB observing configuration only between 2009 August 15 and 2010 December 17.

TABLE 1
DATA-SELECTION SUMMARY

Field	Observed Time (Hours)	Data Percentage		
		ML	PCL	Both
CMB-1	1 855	69.7	64.4	57.7
CMB-2	1 444	73.1	67.1	61.2
CMB-3	1 389	64.4	58.8	52.6
CMB-4	650	72.1	65.4	60.4
Total	5 337	69.5	63.5	57.6

NOTE. — Fraction of data selected for each field by each pipeline. The last column shows the fraction simultaneously selected by both pipelines.

on CMB observations, 14% on Galactic fields²⁷, 13% on calibration sources, and 1% on incomplete observations due to obvious instrumental problems such as a lack of telescope motion. We observed 24 hours per day, except for interruptions due to a variety of factors such as high wind, heavy snow, power outages, and instrumental failures. Our full-season operating efficiency was 63%. For the CMB measurements, we selected four low-foreground sky fields, denoted CMB-1, 2, 3 and 4 (QUIET 2011). In total, we collected 5337 hours of CMB data with the 95-GHz receiver (Table 1).

Each observation consists of a series of constant-elevation scans, hereafter collectively called a CES. The scans are in the azimuth direction with a half amplitude of 7.5° on the sky. Diurnal motion of the sky causes the field to drift through the field of view. After the target has drifted 15° on the sky, we adjust the azimuth and elevation to retrack the field and begin a new CES. Each individual CES thus scans over an area of $\sim 15^\circ \times 15^\circ$. Due to the field of view of $\sim 8^\circ$ and the fact that the sky does not always drift orthogonal to the scan direction, a larger area is observed in practice. The deck angle is changed by 45° each week, providing a large degree of immunity to spurious B -modes induced by I -to- Q/U leakage.

4. CALIBRATION

The instrument calibration procedure for the 95-GHz observations is similar to that used for the 43-GHz data (QUIET 2011; QUIET 2012). The instantaneous beam point-spread function is derived from observations of Taurus A (hereafter Tau A). The resulting beam function has a width of 11.7 FWHM with a small non-Gaussian correction (QUIET 2012). The telescope pointing model is calibrated with a set of astronomical objects: Tau A, Jupiter, RCW 38, the Moon, and the Galactic center. The residual random scatter after applying all pointing corrections is 5.1 FWHM. To correct for this, we convolve the beam window function with the residual-pointing-scatter term, and obtain an effective point-spread function of 12.8 FWHM. The detector angles (i.e., the orientations of the polarization responses) are calibrated to 0.5° precision with the combination of Tau A observations for absolute-angle determination and a sparse-

wire-grid calibrator (Tajima et al. 2012; QUIET 2012) for relative angle determination. The considerable improvement in the detector angle precision compared to the previous 43-GHz analysis (QUIET 2011) is due to a more accurate catalog value of Tau A (Aumont et al. 2010) as well as an improved wire grid calibration. Large and small sky dips (elevation nodes of $\pm 20^\circ$ and $\pm 3^\circ$ amplitudes, respectively) modulate loading from atmospheric emission and allow us to measure the fractional I -to- Q/U monopole leakage with 0.3% precision per calibration, while Jupiter measurements are used to measure the higher-order leakage terms (i.e., dipole and quadrupole) and to confirm the sky-dip monopole-leakage results. The detector responsivities are calibrated using Tau A and sky-dip data as well as the measurement using the sparse wire grid. The typical responsivity is found to be 3.1 mV K^{-1} in antenna temperature units.

5. DATA ANALYSIS

The analysis procedure used for the 95-GHz data reduction follows closely the 43-GHz analysis (QUIET 2011), and we refer the reader to this publication as well as recent Ph. D. theses (Buder 2012; Chinone 2011; Dumoulin 2011; Monsalve 2012; Næss 2012) for full details. We have implemented two independent analysis pipelines, one based on a maximum-likelihood (ML) technique and the other on a pseudo- C_ℓ (PCL) cross-correlation technique. The most important improvements since the previous publication are, for the ML pipeline, an adaptive filter procedure in which the filter parameters depend on the data quality of the specific data segment, as well as a pseudo- C_ℓ null-test estimator, allowing for many more null tests; and, for the PCL pipeline, a different and more robust data division for the cross-correlation²⁸, taking further advantage of the scanning strategy.

The process to extract cosmological results from raw time-ordered data (TOD), containing measurements of the Stokes Q and U parameters as well as the telescope pointing information, can be summarized in three steps: TOD pre-processing, map making, and power-spectrum and parameter estimation. The TOD pre-processing involves estimating and applying calibration factors, characterizing the detector noise, and applying high-pass, low-pass and azimuth filters to minimize the effects of atmospheric fluctuations, far sidelobes, excess high-frequency instrumental noise, and ground pickup. Then, sky maps are generated by projecting the Q and U intensities into Galactic coordinates, taking into account the telescope pointing information, using standard map-making equations (QUIET 2011). Figure 1 shows the maximum-likelihood Stokes Q and U maps of the CMB-1 field generated with the ML pipeline. Power-spectrum estimation is performed with one of two techniques, depending on the pipeline. The ML pipeline implements a standard Newton-Raphson maximum-likelihood solver (Bond et al. 1998), while the PCL pipeline implements the MASTER pseudo- C_ℓ algorithm (Hivon et al. 2002; Hansen & Gorski 2003). Prior to power-spectrum esti-

Different configurations were used between 2009 August 12 and 15 and between 2010 December 17 and 22 to calibrate and characterize the instrument.

²⁷ The analysis of the Galactic observations is in progress (see Wehus (2012) for preliminary maps), and final results will appear in a future publication.

²⁸ We cross-correlate among 40 subsets of data. Each subset corresponds to a specific boresight azimuth and deck range. There are five azimuth and eight deck ranges.

mation, both pipelines mask Centaurus A, and the PCL pipeline also masks Pictor A.

In the following we describe the data selection, analysis validation and systematic-error assessment. In optimizing the analysis configuration, it is important that the optimization process itself does not introduce experimenter biases, for instance by removing purely statistical fluctuations in the data selection. QUIET is the first CMB experiment to have adopted a strict blind-analysis policy (Klein & Roodman 2005), in which all data-selection criteria, filters, and calibrations are adjusted and finalized, and the systematic errors are assessed prior to looking at any cosmological power spectrum. This process was described in detail in QUIET 2011, and we have adopted the same policy for the 95-GHz analysis.

5.1. Data Selection

Each QUIET radiometer provides four output channels (“detector diodes”), resulting in a total of 336 output channels from 84 polarization-sensitive radiometers. We use 308 good channels for analysis (QUIET 2012). Starting from the resulting data for all CESes, we define two different classes of data-selection criteria. In the first class, we impose criteria that select or reject an entire CES. These include the criteria based on atmospheric conditions, instrument malfunctions, or unusual conditions for the temperature regulation in the focal plane. In the second class, we apply selection criteria to individual detector diodes in each CES (CES-diodes). For instance, a CES-diode is rejected if: 1) the measured noise properties show poor agreement with the noise model; 2) the $1/f$ knee frequency is anomalously high; 3) the white-noise level is non-stationary; 4) there are glitches in the time domain or strong spikes in the Fourier domain; or 5) there is evidence of a large scan-synchronous signal.

Table 1 lists the fractions of data that satisfy the criteria and are used for map making and power-spectrum estimation.

5.2. Analysis Validation

Having defined our data-selection criteria and filters, we need to validate the accepted data set and analysis parameters²⁹. Our most valuable tool for this is a so-called null-test suite (QUIET 2011). In each null test, the full data are split into two subsets. From these, we make individual sky maps, m_1 and m_2 , as well as the corresponding difference map, $m_{\text{diff}} \equiv (m_1 - m_2)/2$. By design, the true sky signal cancels in this map, and the result should be consistent with noise. We therefore compute the EE and BB power spectra of this map, and check for consistency with the zero-signal hypothesis by comparing to simulations. In the current analysis, the null suite consists of 32 and 23 tests for the PCL and ML pipelines, respectively, with each test targeting a possible source of signal contamination or miscalibration. These are selected to be highly independent; a statistical correlation between null power spectra of two different null-test divisions is typically 0.05.

²⁹ Note that the data-selection criteria are improved through an iterative process of applying the analysis-validation metrics. In the current analysis, ~ 50 different configurations were considered before reaching the final configuration.

TABLE 2
VALIDATION-TEST SUMMARY

Field	Mean of χ_{null}		Total χ_{null}^2		χ_{null}^2 Outlier	
	ML	PCL	ML	PCL	ML	PCL
CMB-1	0.40	0.26	0.31	0.78	0.63	0.14
CMB-2	0.54	0.46	0.08	0.06	0.02	0.40
CMB-3	0.42	0.74	0.31	0.50	0.72	0.45
CMB-4	0.06	0.08	0.43	0.76	0.80	0.18

NOTE. — Results of the three predefined validation tests using the mean of χ_{null} , the sum of χ_{null}^2 , and the worst outlier of χ_{null}^2 . All values are PTEs defined such that a large deviation from zero results in a small PTE.

For each power-spectrum bin b , we calculate the statistic $\chi_{\text{null}}(b) \equiv C_b^{\text{null}}/\sigma_b$, where C_b^{null} is the observed difference power spectrum and σ_b is a Monte Carlo (MC) based estimate of the corresponding standard deviation. We evaluate both χ_{null} and its square for all b ; χ_{null} is sensitive to systematic biases in the null spectra, while χ_{null}^2 is more responsive to outliers.

Prior to the analysis, we defined three critical tests that had to be passed before continuing to cosmological analysis, based on 1) the mean value of χ_{null} , 2) the sum of χ_{null}^2 , and 3) the maximum of χ_{null}^2 , all computed including the entire suite of EE and BB null power spectra. A given analysis configuration passes when these statistics are consistent with the null hypothesis. Table 2 lists the probabilities to exceed (PTE) for the final configuration, and Figure 2 shows the PTE distribution of χ_{null}^2 . The PTEs are defined such that a large deviation from zero results in a low PTE. This corresponds to two-sided PTEs for the mean of χ_{null} and one-sided PTEs for the total χ_{null}^2 and the χ_{null}^2 outlier. The mean of the χ_{null} distributions over all fields is -0.018 ± 0.015 for the PCL pipeline and 0.003 ± 0.017 for the ML pipeline. We do not detect any bias with our final analysis configuration.

We also generate 1000 random null divisions and compare the widths of the resulting χ_{null} distributions between data and MCs using the PCL pipeline. We find these to be consistent, and we verify our estimate of the statistical uncertainty in each multipole bin with a precision of 3.1%. Finally, we evaluate the differences of non-null spectra among the fields, before looking at individual non-null spectra. These differences are consistent with the hypothesis of statistical isotropy (i.e., each field has the same underlying power spectrum), with a PTE of 0.15.

5.3. Systematic Errors

We study the contributions from instrumental systematic errors using the methodology of QUIET 2011. The main effects considered are 1) uncertainties in absolute responsivity and the window function, 2) I -to- Q/U leakage, 3) uncertainties in polarization angles, relative responsivities, and pointing, and 4) residual contamination from scan-synchronous signals and far sidelobes. In each case, we set up an empirical model of the systematic effect and propagate this through the PCL pipeline. The results from these calculations are summarized in Figure 3.

The most important conclusion is that the systematic errors in the BB spectrum are very small. For the multi-

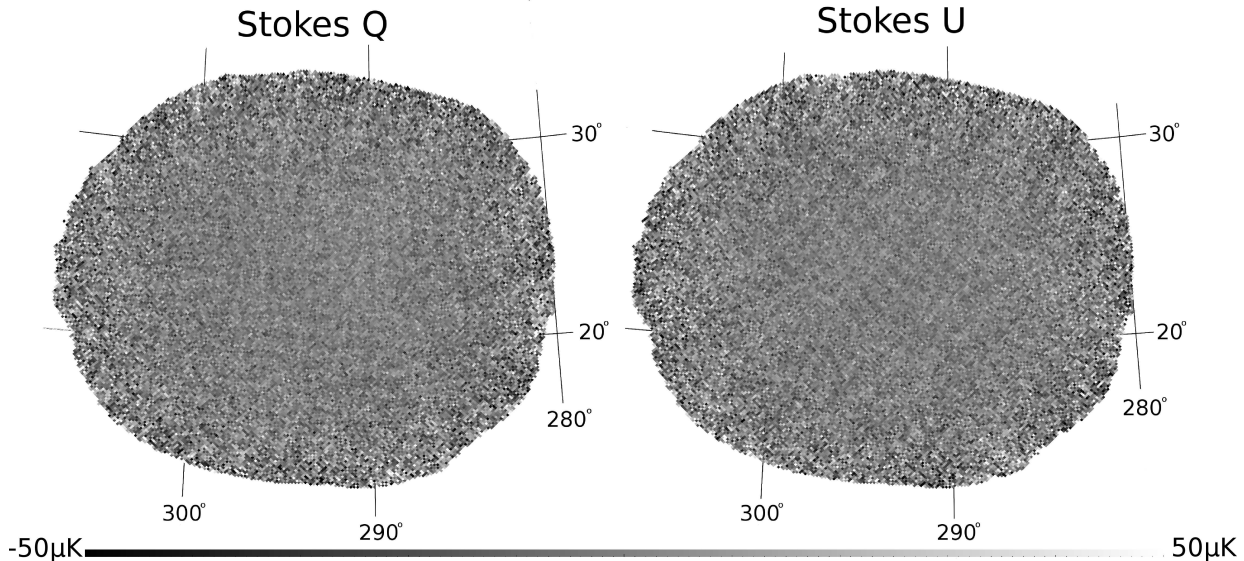


FIG. 1.— QUIET CMB polarization maps of the CMB-1 field in Galactic coordinates at 95 GHz. The left (right) panel shows Stokes Q (U), where the polarization angle is defined with respect to the Galactic North Pole. Note the coherent vertical/horizontal patterns in the Q map, and the diagonal patterns in the U map; these are the expected signature of a pure E -mode signal. No filtering has been applied to this map beyond subtracting the very largest angular scales ($\ell > 25$), to which QUIET is not sensitive.

pole range relevant for estimation of the tensor-to-scalar ratio, $\ell \sim 100$, each effect is smaller than or comparable to the signal corresponding to $r \sim 0.01$, the lowest level ever reported in the literature. It is also noteworthy that this limit improves on that reported for the 43-GHz data ($r < 0.1$; QUIET 2011) by an order of magnitude. This is due to improved rejection of I -to- Q/U leakage, better detector-angle calibration, and lower levels of side-lobe contamination resulting from the installation of the upper parts of the ground screen.

For the EE power spectrum, the systematic error budget is dominated by uncertainties in the multiplicative responsivity calibration. The total uncertainty is 8%, almost equally contributed from three dominant sources: the uncertainty of the polarization flux of Tau A (5%; Weiland et al. 2011), the uncertainty in the beam solid angle (5%), and the uncertainty associated with modeling the time variation and relative responsivity among the detector channels (4%). This translates into an uncertainty of 17% in the power spectrum. For comparison, the statistical uncertainty in the EE spectrum is about 8% of the central value at its minimum around $\ell \sim 400$. It is important to note that the responsivity effect is purely multiplicative and therefore cannot create spurious B -mode signal. The uncertainty of the window function is another multiplicative factor highly correlated among different ℓ bins, with the magnitude dependent on ℓ . The uncertainty comes from both the beam window function and the smearing factor due to the pointing error, and is listed in Table 3. These errors are smaller than the EE statistical uncertainties.

The dominant systematic uncertainty for EB is due to calibration errors in the detector polarization angles. To first approximation, an error in the absolute-polarization-angle calibration of $\delta\psi$ induces a spurious EB spectrum proportional to $\sim C_\ell^{EE} \sin 2\delta\psi$, and a BB spectrum proportional to $\sim C_\ell^{EE} \sin^2 2\delta\psi$. Uncertainties in the relative polarization angles among detectors contribute to the systematic errors in EB and BB spectra in

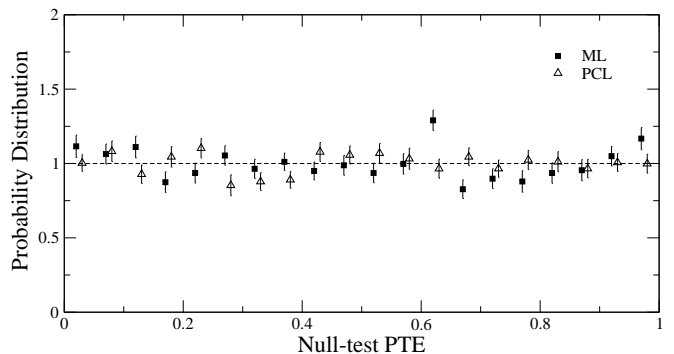


FIG. 2.— Null-test-PTE distributions for χ^2_{null} for both the ML and PCL pipelines. Each is consistent with the uniform expectation.

a similar manner. The calculations summarized in Figure 3 capture both these effects through simulations. As seen in this figure, these polarization-angle uncertainties lead to systematic errors almost as large as the statistical errors for EB around $\ell \sim 400$, while for BB they are small everywhere and comparable to other sources of systematic errors. Table 3 lists the total systematic error for the EB power spectrum.

6. POWER SPECTRA AND COSMOLOGICAL PARAMETERS

The measurements of the EE , EB and BB power spectra are tabulated in Table 3, and plotted in Figure 4. The EE spectrum is strongly signal-dominated up to $\ell \sim 800$, and three acoustic peaks are clearly traced. Both the BB and EB spectra are consistent with zero within the estimated statistical and systematic uncertainties. The dominant EE power is also visible in the maps shown in Figure 1. Note that these maps have not been filtered, except by subtracting the very largest scales ($\ell \lesssim 25$), to which QUIET is not sensitive. One can see a distinct vertical-horizontal coherent pattern on small angular scales in the Stokes Q map, and a similar diagonal pattern in the U map. This is the expected signature of

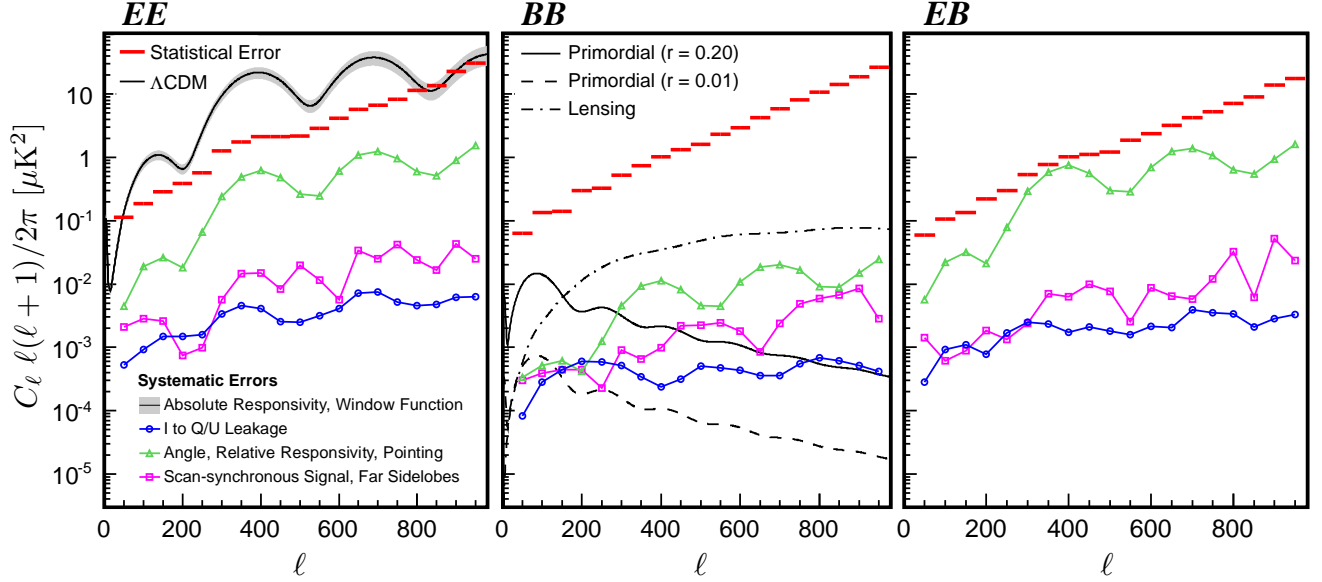


FIG. 3.— Summary of systematic error assessment for EE (left), BB (middle), and EB (right). The red bars indicate the statistical uncertainties in each bin. Blue, green, and purple points correspond to three categories of systematic errors: I -to- Q/U leakage; polarization angles (absolute and relative), relative responsivities and pointing error; and the residual scan-synchronous signals and far sidelobes. The gray band along the Λ CDM curve in EE corresponds to the uncertainties of multiplicative factors: absolute responsivity and the window function. For BB , all systematic errors are below the level of $r \sim 0.01$ at $\ell \sim 100$. For EE the dominant systematic error is uncertainty in the absolute responsivity, which is a purely multiplicative effect. For EB , the dominant systematic is caused by uncertainties in the

an E -mode signal.

The results from the two pipelines are consistent with each other. The most noticeable difference is a single overall multiplicative factor, which is only relevant in evaluating the consistency of the EE power spectra. This factor comes from different responsivity modeling and is consistent with the systematic error budget discussed in Section 5.3.

When assessing the consistency of the EE power spectrum with the Λ CDM prediction, it is convenient to factor the spectrum measurement into an overall amplitude and the spectral shape of the acoustic peaks. We fit a free amplitude, q , relative to the EE spectrum predicted by the best-fit seven-year *WMAP* Λ CDM parameters (Komatsu et al. 2011) to the spectrum from each pipeline, and find $q = 1.22 \pm 0.04(\text{stat})^{+0.22}_{-0.17}(\text{syst})$ and $q = 1.35 \pm 0.05(\text{stat})^{+0.26}_{-0.22}(\text{syst})$ for the PCL and ML pipelines, respectively. These values are consistent with the Λ CDM prediction of $q = 1$, and correspond to PTEs of 0.20 and 0.06, respectively. Figure 5 provides a spectral shape comparison. Here we see that the measured EE spectrum rescaled to $q = 1$ accurately traces the first three acoustic peaks predicted by the Λ CDM model.

We assess the overall consistency with the Λ CDM hypothesis by calculating a total χ^2 relative to Λ CDM (and relative to $C_\ell^{BB} = C_\ell^{EB} = 0$), taking into account the systematic uncertainties due to the responsivity calibration in EE and the systematic error in EB primarily due to detector polarization angles. The former is incorporated by introducing a nuisance parameter for the absolute responsivity constrained by a Gaussian distribution with a standard deviation equal to the assigned systematic error. The latter is incorporated by modeling the EB systematic error as $sC_\ell^{EB,\text{syst}}$, where the scale factor s is constrained by a Gaussian with $\sigma = 1$ and $C_\ell^{EB,\text{syst}}$ is the systematic error estimated in Sec-

tion 5.3; this means we assume the systematic errors are completely correlated among different ℓ bins. The systematic errors in BB are negligibly small. Including the systematic error contributions, we find χ^2 of 67.3 and 70.2 for the PCL and ML pipelines, respectively. With 57 degrees of freedom, these values correspond to PTEs of 0.16 and 0.11, respectively; the derived spectra are consistent with Λ CDM.

Since we find no significant excess in the BB power spectrum, we place an upper limit on possible BB power in each bin. The ML pipeline calculates the upper limit by the 95% integral of the positive part of the likelihood, while the PCL pipeline adopts a frequentist-based hypothesis-testing method. Specifically, the upper limit μ is defined by $0.05 = p(q_\mu > q_\mu^{\text{obs}}|\mu)/p(q_\mu > q_\mu^{\text{obs}}|0)$, where $p(\cdots|\mu)$ and $p(\cdots|0)$ represent p -values of the null hypothesis with power μ and an alternative hypothesis with zero power, respectively. The parameters μ , q_μ and q_μ^{obs} correspond to the bandpower C_b , the test statistic for upper limit defined in Cowan et al. (2011), and the test statistic q_μ calculated for the observed bandpower \hat{C}_b , respectively. Table 3 lists the derived upper limits.

We constrain the tensor-to-scalar ratio r using standard likelihood methods and including only the BB spectrum at low multipoles ($26 \leq \ell \leq 175$). For simplicity, we consider only the amplitude of a BB template computed with the standard Λ CDM concordance parameters, and fix the tensor spectral index to $n_t = 0$ (QUIET 2011; Chiang et al. 2010). In constraining r , the uncertainty of the responsivity calibration is eliminated by simultaneously fitting EE and BB power spectra using the Λ CDM templates. We define the fit function as $C_\ell^{EE}(q) = qC_\ell^{EE,\text{fid}}$ and $C_\ell^{BB}(q, r) = r q C_\ell^{BB,\text{fid}}$. Here $C_\ell^{EE,\text{fid}}$ and $C_\ell^{BB,\text{fid}}$ denote the fiducial Λ CDM EE -power-spectrum template and the BB -power-spectrum

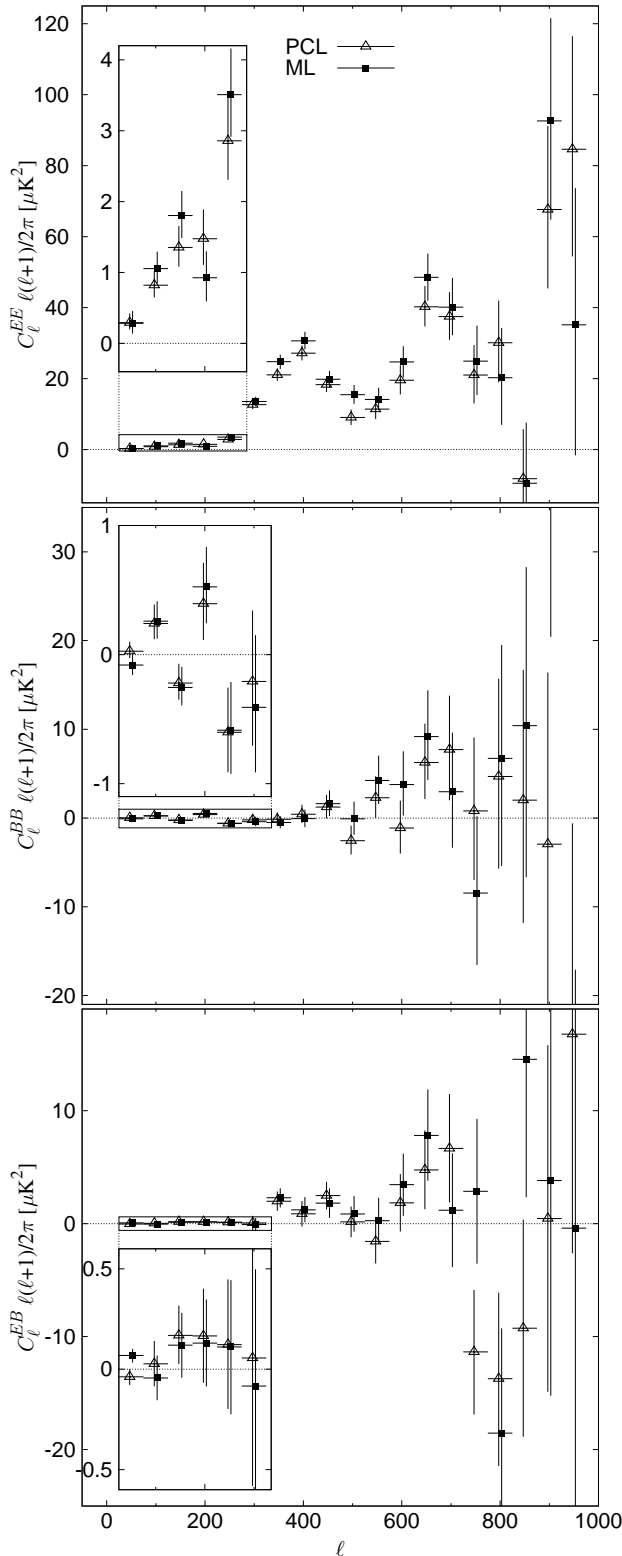


FIG. 4.— The QUIET 95-GHz power spectra, co-added over all four CMB fields. The panels show the EE (top), BB (middle) and EB (bottom) spectra, and the insets show the low- ℓ region in detail. The central ℓ values from the two pipelines are slightly offset for display purposes. Note that the error bars indicate statistical errors only; see Section 5.3 for a discussion of systematic errors. Typical correlations among neighboring bins are ~ -0.1 . The full set of three spectra are consistent with the EE spectrum predicted by the Λ CDM model and $C_\ell^{BB} = C_\ell^{EB} = 0$.

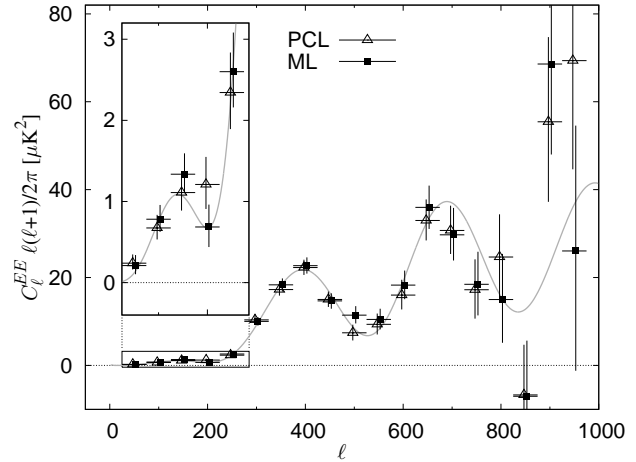


FIG. 5.— Comparison of the QUIET EE spectrum with current best-fit Λ CDM model after scaling the absolute responsivity to $q = 1$. The central ℓ values from the two pipelines are slightly offset for display purposes. Typical correlations among neighboring bins are ~ -0.1 . The results from the two pipelines are consistent, and the shape of the QUIET EE spectrum is in excellent agreement with the Λ CDM model.

template with $r = 1$ and $n_t = 0$, respectively. Note that this does not imply that we use EE power to constrain the tensor modes, as the Λ CDM EE template only contains the scalar contribution. This method exploits the fact that r is by definition a ratio and does not depend on the common overall scaling factor. From the simultaneous fit, the ML pipeline finds $r = 1.1^{+0.9}_{-0.8}$, with a 95% C.L. upper limit of $r < 2.8$, and the PCL pipeline finds $r = 1.2^{+0.9}_{-0.8}$, corresponding to an upper limit of $r < 2.7$. The systematic uncertainty is negligible, at the level of $r = 0.01$.

7. FOREGROUNDS

We assess the level of diffuse foregrounds, in particular synchrotron radiation and dust emission, as additional sources of systematic errors. Contamination from residual point sources is negligible. An estimate using the point-source component of the Planck Sky Model (PSM; Delabrouille et al. 2012, PSM v1.7.4) yields a limit of $C_\ell < 1.4 \times 10^{-6} \mu\text{K}^2$ over the entire ℓ range without masking any sources³⁰. An estimate based on a source-population model (Tucci & Toffolatti 2012) relative to our nominal point-source mask results in an even lower level, $C_\ell \sim 5 \times 10^{-7} \mu\text{K}^2$. Both are well below our statistical uncertainty.

Considering synchrotron radiation, we note that the 43-GHz QUIET observations have already resulted in strong constraints on any synchrotron component in each of the QUIET CMB fields (QUIET 2011). Except for the single case of the EE spectrum at $\ell \leq 75$ measured in CMB-1, no evidence of any contamination was found. These results allow us to constrain any contribution from synchrotron emission at 95 GHz by extrapolation. Adopting a spectral index of $\beta_s = -2.7$ (Dunkley et al. 2009), we estimate the EE (BB) excess power to be $0.011 \pm 0.003 \mu\text{K}^2$ ($0.001 \pm 0.002 \mu\text{K}^2$) for the first bin of the CMB-1 spectrum, which is negligible compared to statistical errors.

In order to constrain contamination from dust emis-

³⁰ Note that this limit is given in units of C_ℓ , not $C_\ell \ell(\ell+1)/2\pi$.

sion, we adopt the thermal-dust component of the PSM as a template; the PSM predicts that other sources of contamination are subdominant at 95 GHz in the QUIET fields. We estimate the dust power contribution in our fields by evaluating both the PSM power spectrum and the PSM-QUIET cross-spectrum using the PCL pipeline. The possible contamination is only relevant in the first bin ($25 \leq \ell \leq 75$) of the field CMB-1. In this bin, the PSM power amplitude is $0.087 \mu\text{K}^2$ ($0.070 \mu\text{K}^2$) for the EE (BB) spectrum, while the corresponding cross power is $0.060 \pm 0.035 \mu\text{K}^2$ ($0.016 \pm 0.027 \mu\text{K}^2$). Taking into account the relative weights of the individual fields, we therefore estimate that the dust-emission contribution to the first EE bin in the final co-added spectrum (Table 3) is $< 0.04 \mu\text{K}^2$, more than a factor two smaller than the statistical uncertainty. All other spectra and multipole ranges have negligible contributions. Fitting the PSM model as a template to CMB-1 in the map domain using the ML pipeline, we find a best-fit amplitude of $A = 0.62 \pm 0.21$. This corresponds to a 3σ correlation with the thermal-dust PSM component, which at the same time agrees with the PSM prediction ($A = 1$) at 1.8σ . Consistent results are obtained by taking the ratio of the cross-power to the PSM power including the full multipole range, with an amplitude of $A = 0.66 \pm 0.25$. The three other fields all have best-fit amplitudes consistent with zero. We note as a caveat that the uncertainty in the PSM itself is not taken into account in this analysis, and the results depend critically on this model as the detected foreground levels are well below the statistical errors of the measured power spectra themselves.

8. CONCLUSIONS

We have presented the CMB polarization power spectra from the 95-GHz QUIET observations. The EE spectrum has been measured between $\ell = 25$ and 975, and the first three acoustic peaks were seen with high signal-to-noise ratio, consistent with ΛCDM predictions. The BB spectrum was found to be consistent with zero, with a 95% C.L. upper limit on the tensor-to-scalar ratio of $r < 2.7$ (PCL) or 2.8 (ML), depending on pipeline. In Figure 6, we provide an up-to-date overview of the current state of the CMB polarization field, comparing the results from various experiments³¹. In one of the fields, we found a correlation with the dust component of the Planck Sky Model. The excess power due to this component was still small compared to the statistical errors of the power spectra. Finally, we have demonstrated the lowest level of instrumental systematic errors to date. We conclude by noting that part of the role of this experiment was to serve as a pathfinder to demonstrate that MMIC arrays were capable of reaching $r \lesssim 0.01$; this has been successfully achieved.

Support for the QUIET instrument and operation comes through the NSF cooperative agreement AST-0506648. Support was also provided by NSF awards PHY-0355328, AST-0448909, PHY-0551142,

³¹ For the EE spectrum of QUIET, we show the mean of the spectrum from the two pipelines (after scaling to $q = 1$) as a succinct visualization. For BB , the results from the two individual pipelines are indicated by the vertical extent of the QUIET-W points.

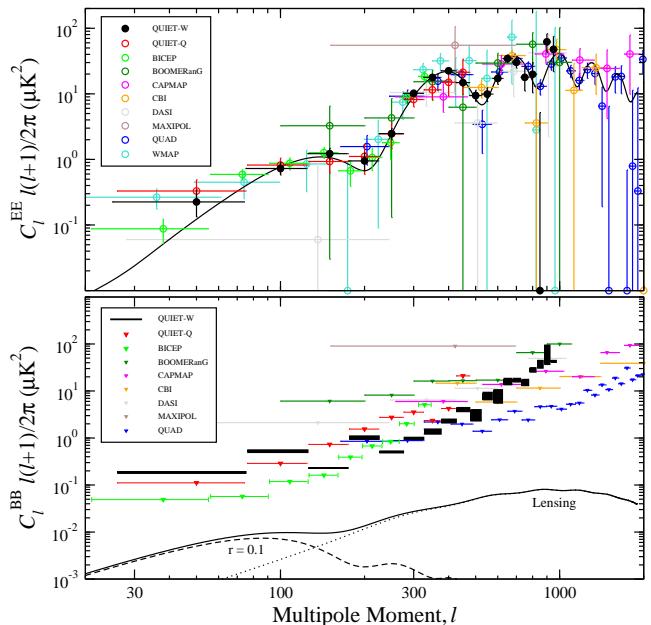


FIG. 6.— Summary of published CMB polarization EE power spectrum (top) and 95% C.L. upper limits on BB power (bottom) measured by different experiments (Leitch et al. 2005; Montroy et al. 2006; Sievers et al. 2007; Wu et al. 2007; Bischoff et al. 2008; Brown et al. 2009; Chiang et al. 2010; Larson et al. 2011; QUIET 2011) as well as the result reported in this paper (QUIET-W). The QUIET-W points, spanning the first three acoustic peaks in the EE power spectrum, bridge the large ($\ell \lesssim 200$) and small ($\ell \gtrsim 400$) angular-scale measurements made by previous experiments. For visualization purposes, the mean of two pipeline spectra (scaled to $q = 1$) is shown for QUIET-W for EE . For BB , the results from the two individual pipelines are indicated by the vertical extent of the QUIET-W points. The solid line in the upper panel shows the ΛCDM EE spectrum; the dashed and dotted lines in the bottom panel show the BB spectrum from gravitational waves (for $r = 0.1$) and lensing, respectively.

PHY-0855887, and AST-1010016; KAKENHI 20244041, 20740158, and 21111002; PRODEX C90284; a KIPAC Enterprise grant; and by the Strategic Alliance for the Implementation of New Technologies (SAINT).

Some work was performed on the Joint Fermilab-KIPAC Supercomputing Cluster, supported by grants from Fermilab, the Kavli Institute for Cosmological Physics, and the University of Chicago. Some work was performed on the Titan Cluster, owned and maintained by the University of Oslo and NOTUR (the Norwegian High Performance Computing Consortium), and on the Central Computing System, owned and operated by the Computing Research Center at KEK. This research used resources of the National Energy Research Scientific Computing Center, which is supported by the Office of Science of the U.S. Department of Energy under Contract No. DE-AC02-05CH11231. Portions of this work were performed at the Jet Propulsion Laboratory (JPL) and California Institute of Technology, operating under a contract with the National Aeronautics and Space Administration. The Q-band modules were developed using funding from the JPL R&TD program. We acknowledge the Northrop Grumman Corporation for collaboration in the development and fabrication of HEMT-based cryogenic temperature-compatible MMICs. We acknowledge the use of the Planck Sky Model, developed by the Component Separation Working Group (WG2) of the Planck Collaboration. Some of the results in this paper have

been derived using the HEALPix (Gorski et al. 2005) software and analysis package.

C.D. acknowledges an STFC Advanced Fellowship and an ERC IRG grant under FP7. R.B. acknowledges support from CONICYT project Basal PFB-06 and alma-conicyt 31070015. A.D.M. acknowledges a Sloan foundation fellowship. H.K.E. acknowledges an ERC Starting Grant under FP7.

PWV measurements were provided by the Atacama Pathfinder Experiment (APEX). We thank CONICYT for granting permission to operate within the Chajnantor Scientific Preserve in Chile, and ALMA for providing site infrastructure support. Field operations were based at the Don Esteban facility run by Astro-Norte. We are particularly indebted to the engineers and technicians who maintained and operated the telescope: José Cortés, Cristóbal Jara, Freddy Muñoz, and Carlos Verdugo.

In addition, we would like to acknowledge the following people for their assistance in the instrument design, con-

struction, commissioning, operation, and in data analysis: Augusto Gutierrez Aitken, Colin Baines, Phil Bannister, Hannah Barker, Matthew R. Becker, Alex Blein, Mircea Bogdan, April Campbell, Anushya Chandra, Sea Moon Cho, Joelle Cooperrider, Mike Crofts, Emma Curry, Maire Daly, Richard Davis, Fritz Dejongh, Joy Didier, Greg Dooley, Hans Eide, Pedro Ferreira, Jonathon Goh, Will Grainger, Peter Hamlington, Takeo Higuchi, Seth Hillbrand, Christian Holler, Ben Hooberman, Kathryn D. Huff, William Imbriale, Oliver King, Eiichiro Komatsu, Jostein Kristiansen, Richard Lai, David Leibovitch, Erik Leitch, Kelly Lepo, Siqi Li, Martha Malin, Mark McCulloch, Steve Meyer, Oliver Montes, David Moore, Ian O'Dwyer, Gustavo Orellana, Stephen Osborne, Stephen Padin, Felipe Pedreros, Ashley Perko, Alan Robinson, Jacklyn Sanders, Dale Sanford, Yuniior Savon, Mary Soria, Alex Sugarbaker, David Sutton, Matias Vidal, Liza Volkova, Edward Wollack, Stephanie Xenos, Octavio Zapata, Mark Zaskowski and Joseph Zuntz.

REFERENCES

- Anderson, L., Aubourg, E., Bailey, S., et al. 2012, arXiv:1203.6594v1 [astro-ph.CO]
- Aumont, J., et al. 2010, A&A, 514, A70
- Bischoff, C., Hyatt, L., McMahon, J. J., et al. 2008, ApJ, 684, 771
- Bischoff, C. A. 2010, Ph.D. Thesis, University of Chicago
- Bond, J. R., Jaffe, A. H., & Knox, L. 1998, Phys. Rev. D, 57, 2117
- Boyle, L. A., Steinhardt, P. J., & Turok, N. 2006, Phys. Rev. Lett., 96, 111301
- Brizius, A. R. 2011, Ph.D. Thesis, University of Chicago
- Brown, M. L., et al. 2009, ApJ, 705, 978
- Buder, I. D. 2012, Ph.D. Thesis, University of Chicago
- Chiang, H. C., Ade, P. A. R., Barkats, D., et al. 2010, ApJ, 711, 1123
- Chinone, Y. 2011, Ph.D. Thesis, Tohoku University
- Cleary, K. A. 2010, Proc. SPIE, 7741, 77412H
- Cowan, G., Cranmer, K., Gross, E., & Vitells, O. 2011, European Physical Journal C, 71, 1554
- Delabrouille, J., et al. 2012, A&A, in preparation
- Dumoulin, R. N. 2011, Ph.D. Thesis, Columbia University
- Dunkley, J., Spergel, D. N., Komatsu, E., et al. 2009, ApJ, 701, 1804
- Dunkley, J., Hlozek, R., Sievers, J., et al. 2011, ApJ, 739, 52
- Gorski, K. M., et al. 2005, ApJ, 622, 759, <http://healpix.jpl.nasa.gov/>
- Hansen, F. K., & Gorski, K. M. 2003, MNRAS, 343, 559
- Hicken, M., Wood-Vasey, W. M., Blondin, S., et al. 2009, ApJ, 700, 1097
- Hivon, E., Gorski, K. M., Netterfield, C. B., et al. 2002, ApJ, 567, 2
- Kamionkowski, M., Kosowsky, A., & Stebbins, A. 1997, Phys. Rev. Lett., 78, 2058
- Keisler, R., Reichardt, C. L., Aird, K. A., et al. 2011, ApJ, 743, 28
- Kessler, R., Becker, A. C., Cinabro, D., et al. 2009, ApJS, 185, 32
- Klein, J. R., & Roodman, A. 2005, Annual Review of Nuclear and Particle Science, 55, 141
- Komatsu, E., Smith, K. M., Dunkley, J., et al. 2011, ApJS, 192, 18
- Kusaka, A. 2010, Proceedings of the 45th Rencontre de Moriond
- Larson, D., Dunkley, J., Hinshaw, G., et al. 2011, ApJS, 192, 16
- Leitch, E. M., Kovac, J. M., Halverson, N. W., et al. 2005, ApJ, 624, 10
- Liddle, A. R., & Lyth, D. H. 2000, Cosmological Inflation and Large-Scale Structure (UK: Cambridge University Press)
- Monsalve, R. 2012, Ph.D. Thesis, University of Miami
- Monsalve, R. A. 2010, Proc. SPIE, 7741, 77412M
- Montroy, T. E., Ade, P. A. R., Bock, J. J., et al. 2006, ApJ, 647, 813
- Næss, S. K. 2012, Ph.D. Thesis, University of Oslo
- Newburgh, L. 2010, Ph.D. Thesis, Columbia University
- Newburgh, L. 2012, in Twelfth Marcel Grossmann Meeting on General Relativity, 2145
- Padin, S., et al. 2002, PASP, 114, 83
- QUIET Collaboration. 2012, submitted to ApJ
- QUIET Collaboration, et al. 2011, ApJ, 741, 111
- Reeves, R. 2012, Journal of Low Temperature Physics, 167, 929
- Rozo, E., Wechsler, R. H., Rykoff, E. S., et al. 2010, ApJ, 708, 645
- Seljak, U., & Zaldarriaga, M. 1997, Phys. Rev. Lett., 78, 2054
- Sievers, J. L., Achermann, C., Bond, J. R., et al. 2007, ApJ, 660, 976
- Tajima, O., Nguyen, H., Bischoff, C., et al. 2012, Journal of Low Temperature Physics, 167, 936
- Tucci, M., & Toffolatti, L. 2012, arXiv:1204.0427v1 [astro-ph.CO]
- Wehus, I. K. 2012, Proc. 23rd Rencontres de Blois: Particle Physics and Cosmology
- Weiland, J. L., Odegard, N., Hill, R. S., et al. 2011, ApJS, 192, 19
- Wu, J. H. P., Zuntz, J., Abroe, M. E., et al. 2007, ApJ, 665, 55

TABLE 3
QUIET POLARIZATION POWER SPECTRA

ML Pipeline				PCL Pipeline		Syst.
ℓ_{\min}	ℓ_{\max}	EE	EE/q	EE	EE/q	Window Function
26	75	$0.28^{+0.17}_{-0.14}$	$0.21^{+0.13}_{-0.11}$	$0.29^{+0.13}_{-0.10}$	$0.24^{+0.11}_{-0.08}$	0.00
76	125	$1.06^{+0.24}_{-0.21}$	$0.78^{+0.18}_{-0.16}$	$0.82^{+0.20}_{-0.17}$	$0.67^{+0.16}_{-0.14}$	0.01
126	175	$1.80^{+0.35}_{-0.32}$	$1.34^{+0.26}_{-0.23}$	$1.35^{+0.30}_{-0.27}$	$1.11^{+0.25}_{-0.22}$	0.01
176	225	$0.93^{+0.37}_{-0.33}$	$0.69^{+0.28}_{-0.25}$	$1.48^{+0.41}_{-0.37}$	$1.21^{+0.34}_{-0.30}$	0.02
226	275	$3.5^{+0.7}_{-0.6}$	$2.6^{+0.5}_{-0.4}$	$2.9^{+0.6}_{-0.5}$	$2.3^{+0.5}_{-0.5}$	0.02
276	325	$13.5^{+1.3}_{-1.3}$	$10.0^{+1.0}_{-1.0}$	$12.7^{+1.3}_{-1.2}$	$10.4^{+1.1}_{-1.0}$	0.03
326	375	$24.8^{+2.0}_{-2.1}$	$18.3^{+1.5}_{-1.5}$	$21.1^{+1.8}_{-1.7}$	$17.3^{+1.5}_{-1.4}$	0.04
376	425	$30.6^{+2.6}_{-2.4}$	$22.7^{+1.9}_{-1.8}$	$27.2^{+2.2}_{-2.1}$	$22.3^{+1.8}_{-1.7}$	0.05
426	475	$19.8^{+2.3}_{-2.4}$	$14.7^{+1.7}_{-1.8}$	$18.3^{+2.2}_{-2.1}$	$15.0^{+1.8}_{-1.7}$	0.05
476	525	$15.5^{+2.7}_{-2.6}$	$11.5^{+2.0}_{-1.9}$	$9.1^{+2.3}_{-2.1}$	$7.4^{+1.9}_{-1.7}$	0.06
526	575	$14.1^{+3.3}_{-3.1}$	$10.5^{+2.4}_{-2.3}$	$11.4^{+3.0}_{-2.8}$	$9.3^{+2.5}_{-2.3}$	0.07
576	625	$24.7^{+4.5}_{-4.3}$	$18.3^{+3.3}_{-3.2}$	$19.5^{+4.2}_{-4.0}$	$16.0^{+3.5}_{-3.3}$	0.08
626	675	49^{+7}_{-7}	36^{+5}_{-5}	40^{+6}_{-6}	33^{+5}_{-5}	0.09
676	725	40^{+8}_{-8}	30^{+6}_{-6}	37^{+7}_{-7}	31^{+6}_{-5}	0.10
726	775	25^{+10}_{-10}	18^{+7}_{-7}	21^{+8}_{-8}	17^{+7}_{-7}	0.11
776	825	20^{+14}_{-13}	15^{+10}_{-10}	30^{+12}_{-11}	25^{+10}_{-9}	0.12
826	875	-9^{+17}_{-16}	-7^{+13}_{-12}	-8^{+14}_{-13}	-7^{+11}_{-11}	0.14
876	925	93^{+29}_{-28}	69^{+21}_{-21}	68^{+24}_{-22}	55^{+19}_{-18}	0.15
926	975	35^{+39}_{-37}	26^{+29}_{-27}	85^{+32}_{-30}	69^{+26}_{-25}	0.17
		$q = 1.35 \pm 0.05^{+0.26}_{-0.22}$		$q = 1.22 \pm 0.04^{+0.22}_{-0.17}$		
ℓ_{\min}	ℓ_{\max}	BB (95% UL)	EB	BB (95% UL)	EB	EB syst.
26	75	$-0.08^{+0.10}_{-0.08}$ (0.19)	$0.07^{+0.03}_{-0.04}$	$0.03^{+0.07}_{-0.05}$ (0.18)	$-0.04^{+0.04}_{-0.04}$	± 0.01
76	125	$0.26^{+0.15}_{-0.14}$ (0.55)	$-0.04^{+0.11}_{-0.11}$	$0.24^{+0.15}_{-0.12}$ (0.50)	$0.03^{+0.11}_{-0.11}$	± 0.02
126	175	$-0.25^{+0.16}_{-0.14}$ (0.23)	$0.12^{+0.16}_{-0.16}$	$-0.22^{+0.15}_{-0.13}$ (0.23)	$0.17^{+0.15}_{-0.14}$	± 0.03
176	225	$0.53^{+0.31}_{-0.28}$ (1.09)	$0.13^{+0.22}_{-0.22}$	$0.39^{+0.32}_{-0.28}$ (0.95)	$0.17^{+0.24}_{-0.23}$	± 0.02
226	275	$-0.59^{+0.37}_{-0.34}$ (0.52)	$0.11^{+0.33}_{-0.34}$	$-0.60^{+0.35}_{-0.31}$ (0.49)	$0.12^{+0.33}_{-0.32}$	± 0.08
276	325	$-0.4^{+0.6}_{-0.5}$ (1.0)	$-0.1^{+0.6}_{-0.6}$	$-0.2^{+0.5}_{-0.5}$ (1.0)	$0.1^{+0.6}_{-0.6}$	± 0.29
326	375	$-0.5^{+0.7}_{-0.7}$ (1.2)	$2.3^{+0.8}_{-0.9}$	$-0.1^{+0.8}_{-0.7}$ (1.5)	$2.0^{+0.9}_{-0.8}$	± 0.59
376	425	$-0.1^{+1.0}_{-1.0}$ (2.1)	$1.2^{+1.1}_{-1.1}$	$0.4^{+1.1}_{-1.0}$ (2.5)	$0.9^{+1.1}_{-1.1}$	± 0.75
426	475	$1.6^{+1.5}_{-1.4}$ (4.4)	$1.8^{+1.3}_{-1.3}$	$1.2^{+1.4}_{-1.3}$ (3.7)	$2.5^{+1.2}_{-1.2}$	± 0.55
476	525	$-0.1^{+1.9}_{-1.8}$ (4.0)	$0.9^{+1.6}_{-1.6}$	$-2.5^{+1.7}_{-1.6}$ (2.3)	$0.2^{+1.4}_{-1.3}$	± 0.30
526	575	$4.2^{+2.8}_{-2.7}$ (9.2)	$0.3^{+2.0}_{-2.0}$	$2.3^{+2.4}_{-2.3}$ (6.6)	$-1.6^{+1.9}_{-2.0}$	± 0.28
576	625	$3.8^{+3.7}_{-3.5}$ (10.5)	$3.4^{+2.7}_{-2.8}$	$-1.1^{+3.1}_{-2.9}$ (5.6)	$1.8^{+2.6}_{-2.5}$	± 0.70
626	675	$9.2^{+5.2}_{-4.9}$ (18.3)	$7.8^{+4.1}_{-4.0}$	$6.3^{+4.4}_{-4.1}$ (13.8)	$4.8^{+3.5}_{-3.5}$	± 1.25
676	725	3^{+7}_{-6} (16)	1^{+5}_{-5}	8^{+6}_{-6} (18)	$6.7^{+4.8}_{-4.8}$	± 1.40
726	775	-8^{+9}_{-8} (13)	3^{+6}_{-6}	1^{+8}_{-8} (17)	-11^{+5}_{-6}	± 1.06
776	825	7^{+13}_{-12} (31)	-19^{+9}_{-9}	5^{+11}_{-10} (26)	-14^{+8}_{-8}	± 0.68
826	875	10^{+18}_{-17} (44)	15^{+12}_{-12}	2^{+15}_{-14} (31)	-9^{+10}_{-10}	± 0.55
876	925	46^{+27}_{-26} (93)	4^{+19}_{-19}	-3^{+19}_{-18} (37)	0^{+15}_{-15}	± 0.93
926	975	-52^{+35}_{-33} (44)	0^{+25}_{-25}	-28^{+27}_{-26} (41)	17^{+19}_{-19}	± 1.59

NOTE. — Tabulated values are given in CMB thermodynamic units of μK^2 , scaled as $C_\ell \ell(\ell+1)/2\pi$. We present the results from both the ML and PCL pipelines; they are in excellent statistical agreement. The column EE/q shows the EE power spectrum normalized to $q = 1$, as plotted in Figure 5. The fit value of q is also shown in the table, where the first and second errors are statistical and systematic, respectively. The column of BB -power-spectrum values also provides 95% confidence level upper limits in parentheses. We also list two relevant systematic-error contributions besides the uncertainty from the responsivity calibration: the fractional error due to the uncertainty of the beam window function, and the total systematic error in the EB power spectrum in units of μK^2 . Note that they are both highly correlated among ℓ bins.